Cortical response selectivity derives from strength in numbers of synapses

Benjamin Scholl[1,3,*], **Connon I. Thomas**[2,*], **Melissa A. Ryan**[2], **Naomi Kamasawa**[2], **David Fitzpatrick**[1]

[1]Functional Architecture and Development of Cerebral Cortex, Max Planck Florida Institute for Neuroscience, 1 Max Planck Way, Jupiter, FL 33458, USA

[2]Electron Microscopy Core Facility, Max Planck Florida Institute for Neuroscience, 1 Max Planck Way, Jupiter, FL 33458, USA

[3]Present address: Department of Neuroscience, Perelman School of Medicine at the University of Pennsylvania, 415 Curie Blvd, Philadelphia, PA, 19104, USA

Abstract

Single neocortical neurons are driven by populations of excitatory inputs, forming the basis of neuronal selectivity to features of sensory input. Excitatory connections are thought to mature during development through activity-dependent Hebbian plasticity[1], whereby similarity between presynaptic and postsynaptic activity selectively strengthens some synapses and weakens others[2]. Evidence in support of this process ranges from measurements of synaptic ultrastructure to *in vitro* and *in vivo* physiology and imaging studies[3,4,5,6,7,8]. These corroborating lines of evidence lead to the prediction that a small number of strong synaptic inputs drive neuronal selectivity, while weak synaptic inputs are less correlated with the somatic output and modulate activity overall[6,7]. Supporting evidence from cortical circuits, however, has been limited to measurements of neighboring, connected cell pairs, raising the question of whether this prediction holds for a broad range of synapses converging onto cortical neurons. Here we measure the strengths of functionally characterized excitatory inputs contacting single pyramidal neurons in ferret primary visual cortex (V1) by combining *in vivo* two-photon synaptic imaging and *post hoc* electron microscopy (EM). Using EM reconstruction of individual synapses as a metric of strength, we find no evidence that strong synapses play a predominant role in the selectivity of cortical neuron responses to visual stimuli. Instead, selectivity appears to arise from the total number of synapses activated by different stimuli. Moreover, spatial clustering of co-active inputs appears reserved for weaker synapses, enhancing the contribution of weak synapses to somatic responses. Our results challenge the role of Hebbian mechanisms in shaping neuronal selectivity in cortical circuits, and suggest

that selectivity reflects the co-activation of large populations of presynaptic neurons with similar properties and a mixture of strengths.

We measured visually-driven activity and ultrastructural anatomy of the same synapses on single cortical neurons in ferret V1 (Extended Data Fig. 1, Supplementary Data 1; Methods). We first performed *in vivo* two-photon imaging of single layer 2/3 pyramidal neurons and dendritic spines on proximal basal dendrites expressing a genetically-encoded activity reporter (GCaMP6s)[9] to measure functional activity. Following *in vivo* imaging, we perfused the tissue under fixation, sectioned tangential to the imaging plane, and prepared the tissue for serial block-face scanning electron microscopy (SBF-SEM, Methods)[10]. After identifying the location of imaged cells, we performed high-resolution SBF-SEM (Extended Data Table 1). We manually reconstructed the volume of an imaged cell's soma, dendrites, and spines (Fig. 1a). For each synapse we reconstructed the spine head, neck, postsynaptic density (PSD), and presynaptic bouton (Fig. 1b). Compared with two-photon imaging, synaptic ultrastructure was complex and diverse[11,12] (Fig. 1b). Visually-driven activity ($\Delta F/F_o$) from these spines exhibited co-tuning or differential-tuning with respect to the soma (Fig. 1c-d), as reported previously[9,13].

We reconstructed 155 visually-responsive (Methods) synapses imaged *in vivo* on 23 dendritic segments from 5 cells. Most spines (98.7%, n = 153/155) received input from a single presynaptic bouton such that synapses were 'one-to-one' connections. A majority (70.0%, n = 109/155) had perforated PSDs, evident by discontinuities across serial EM sections[14]. Synapse anatomical features varied in size (Spine head volume: mean = 0.39 ± 0.30 μm^3 s.d.; PSD area: mean = 0.29 ± 0.22 μm^2 s.d.; Bouton volume: mean = 0.33 ± 0.26 μm^3 s.d.; Neck length: mean = 1.87 ± 0.86 μm s.d.). Spine head volume was strongly correlated with PSD area, but not neck length (Extended Data Fig. 2)[11]. To identify whether GCaMP6s expression altered synapse size, we reconstructed all spines in a subset of labeled and unlabeled dendrites. Combining target and non-target spines (n = 114) and comparing reconstructions on unlabeled dendrites (n = 71) we found no difference in volume (labeled: mean = 0.27 ± 0.36 μm^3 s.d.; unlabeled: mean = 0.19 ± 0.20 μm^3 s.d.; p = 0.55; Wilcoxon rank-sum two-sided test).

For comparison with EM features, we calculated functional metrics from peak $\Delta F/F_o$ responses for each spine (Methods). Spines exhibited diverse preferences for direction, orientation, and ocular dominance, rather than strictly matching the soma (absolute preference difference ranges = 179.2°, 89.0°, and 1.48 respectively; Extended Data Fig. 2). Similarly, there was a wide range in spine selectivity for direction and orientation (0.79 and 0.80, respectively, Methods), despite little variation in somatic tuning selectivity (Direction: 0.21 ± 0.09, Orientation: 0.48 ± 0.04, mean ± s.e., n = 5). In sum, the populations of synaptic inputs on individual cells exhibit both a wide range of strengths (small and large) and functional properties (aligned and misaligned to the soma), raising the question whether there is a systematic functional synaptic weight distribution.

To test whether strong synaptic inputs drive neuronal selectivity and are co-tuned to the soma, we compared synapse structural and functional properties. For simplicity, we first focus on orientation preference. Surprisingly, the strength of individual synapses was

uncorrelated with functional similarity to the somatic output (i.e. absolute orientation preference difference) (Fig. 2). We found no relationship for spine head volume or PSD area (Fig. 2a-b). These results held when using an alternative method to isolate spine signals (Methods; Volume circular-linear $r = 0.12$, $p = 0.70$; PSD area circular-linear $r = 0.20$, $p = 0.39$; one-sided tests). Similarity in orientation preference and PSD area did not depend on spine distance from the soma (< 50 µm: $p = 0.99$, $n = 77$; > 50 µm: $p = 0.84$, $n = 78$; Wilcoxon rank-sum two-sided test). We also found no relationship between orientation preference and spine neck length (Circular-linear $r = 0.07$, $p = 0.66$, one-sided test) or the PSD area/neck length ratio (Circular-linear $r = 0.08$, $p = 0.62$, one-sided test).

Because PSD area is a structural correlate of synaptic strength[15,16], spine necks can attenuate presynaptic drive[17], and these two features are uncorrelated with each other (Extended Data Fig. 2), we generated a separate metric to account for the interaction of all anatomical features using a NEURON model[18] (Methods). For each synapse we simulated depolarization in spine and soma compartments after a single presynaptic spike (Extended Data Fig. 2). Even for simulated somatic depolarization, we uncovered no systematic relationship (Fig. 2c). Null relationships were also found for direction preference, ocular dominance, and spine-soma tuning correlation (Extended Data Fig. 3). To ensure our results are accurate, we tightened inclusion criteria and performed the same analyses. Spines exhibiting low residual-correlation with global dendritic events ($r < 0.2$, $n = 75$) or high signal-to-noise ratio (SNR > 3, $n = 71$) exhibited no correlation between any functional or anatomical property examined (Extended Data Figs. 4-5). Even when analyzing spine populations from individual cells, we observed no relationships (Extended Data Fig. 6). These data suggest that strong and weak synapses on individual neurons are equally likely to be functionally similar or dissimilar to the somatic output.

How might synaptic populations contribute to selectivity without functionally-biased synaptic weight distributions? We propose that a major factor contributing to selectivity is the total number of synapses recruited. To examine this possibility we compared synaptic aggregate predictions with the average somatic orientation tuning across our 5 cells, focusing on dominant-eye stimuli. As spine F/F_o does not reflect strength[19] and PSD area was uncorrelated with F/F_o amplitude (Spearman's $r = 0.07$, $p = 0.19$, one-sided test), we converted spine F/F_o into discrete calcium events (Methods). We defined 'active' synapses as those with calcium events in $\geq 50\%$ of trials for a particular stimulus. Total average synaptic weight was calculated by summing PSD area across active synapses for each stimulus orientation ($\pm 67.5°$ around somatic preference). Total weight was selective for the somatic preferred orientation (Fig. 3a), however, a main determinant for this selectivity was the *total number* of active synapses contributing to each stimulus condition (Fig. 3a-b), which was normally distributed about the somatic preference ($p = 0.36$, Lilliefors test). No differential recruitment of strength was evident across stimuli (Fig. 3b; $p = 0.52$, Kruskal-Wallis test). Thus, synaptic aggregate tuning is due, in part, to an overrepresentation of somatic preference (Extended Data Fig. 2f), leading to increased numbers of synapses recruited for preferred stimuli. These observations were consistent for a range of cutoff values defining 'active' spines (event reliability $20 - 80\%$) and the majority of cell's synaptic populations in this study ($n = 4/5$; $p \geq 0.37$, Lilliefors test; $p \geq 0.31$, Kruskal-Wallis test). Our data do not support the hypothesis that the strongest synaptic inputs contribute

disproportionally to somatic selectivity. Instead, they reveal the importance of strength in numbers of synapses recruited by sensory stimuli.

Another factor contributing to neuronal selectivity is spatial clustering of co-active synapses. Combined strength through co-activity is enhanced by spatial proximity[20], and functionally-similar, neighboring co-active synapses[9] are proposed to exhibit greater strength through cooperative plasticity[21]. It is unknown, however, if synaptic clustering relates to strength. We first computed distance-dependent trial-to-trial correlations between pairs of synapses across all visual stimuli[9] (Fig. 4a). We then restricted pairwise comparisons to either weak or strong synapses (volume cutoff = 0.35 μm^3). Functional clustering was evident for weaker synapses, not stronger synapses (Fig. 4b-c). In addition, functional clustering of weaker inputs persisted for spines co-tuned with their corresponding soma (Fig. 4d). These findings were supported by a linear regression model predicting pairwise correlations based on spine distance, overall size, size similarity, and spine-soma orientation similarity (Extended Data Table 2, Methods). Excluding stimulus trials containing dendritic calcium events produced similar results (Extended Data Fig. 7, Methods). Extending these analyses to synapse pairs with short or long spine necks (1.75 μm cutoff), we observed no differences between groups (Extended Data Fig. 7). Taken together, these analyses suggest that larger (stronger) synapses are more spatially-isolated in activity and the spatiotemporal clustering of smaller (weaker) synapses might act to enhance their combined synaptic strength in numbers.

Correlating *in vivo* synaptic imaging and EM to measure functional properties and anatomical strength, we tested a hypothesis that strong synaptic inputs drive selectivity, while weak synaptic inputs are not structured and act to modulate activity overall[6,7]. We found no evidence to support this hypothesis. Instead our data suggest that selectivity derives from the total number of active synapses, including weak and strong. Greater excitatory drive accompanying presentation of a preferred stimulus reflects activation of a greater number of synapses (Fig. 4e). Weaker synapses are greater in number overall as synaptic strength is lognormally distributed[22] and spatial clustering may act to enhance their effect on somatic activity. Notably, we likely underestimate the total number of synapses contributing to the somatic output, due to our inclusion criteria and removal of back-propagating action potentials. Spines targeted for reconstruction by *in vivo* two-photon imaging were also larger than non-targets on the same branch (target volume: mean = 0.38 ± 0.25 μm^3 s.d., n = 26; non-target volume: mean = 0.24 ± 0.39 μm^3 s.d., n = 88; p = 0.000073, Wilcoxon rank-sum two-sided test), indicating an under sampling of weaker spines overall.

One possible explanation for our observations is that postsynaptic spiking activity shapes the overall distribution of input functional properties, rather than modulating unitary synapse strength. This would give rise to soma-biased input populations[9,13] and could be achieved by modulating synaptogenesis and synaptic pruning[23]; increasing the probability of stabilizing inputs co-tuned with the somatic output. While developmental models have made similar predictions[24], this process has not been observed *in vivo*. How the strength of individual synapses relates to visual processing remains unclear, but this may be constrained by other operational features distinguishing presynaptic afferents. In fact, when comparing spine tuning selectivity with anatomical correlates of strength we did find significant correlations (Extended Data Fig. 8). Thus, synaptic strength may reflect afferent reliability in

representing particular visual features or dynamic range in spike rate. Synaptic strength in this case might not follow Hebbian spike-timing-dependent-plasticity[2], but instead, depend on non-Hebbian plasticity[25] or local signaling mechanisms[26].

Why do our measurements differ from previous studies? First, no previous study has assessed functional and anatomical properties of a population of excitatory synapses converging onto single cortical neurons. Synaptic strength is conventionally defined by somatic EPSP amplitude recorded with electrophysiology[27–29]. Somatic EPSPs result from both the number[27–29] and strength of presynaptic contacts[30], as well as somatic proximity. Further, the difficulty of such measurements leads to a bias for identifying connections between nearby neurons, as opposed to our approach which includes dendritic inputs whose presynaptic partner may reside locally or project long-range. Local sampling could explain different conclusions derived from experiments using correlative EM and cellular imaging to assess connectivity between nearby layer 2/3 neurons[7]. Fundamental differences in circuit design between rodents and carnivores may contribute to differences. We also cannot exclude the possibility of a weak functional bias in synaptic strength given biological variability, measurement noise, and our sample size; however our dataset would have sufficient statistical power to detect previously reported correlations7 (Supplementary Data 2). Clearly, there is more to be learned about the synaptic weight distributions of cortical neurons, including whether they vary for different sources of inputs and different dendritic compartments[31]. Our results suggest that functionally-biased synaptic weight is not the primary factor determining response selectivity, challenging prevailing views of the developmental mechanisms shaping selectivity.

Data availability

An example EM image volume is publicly available: https://mpfi.org/download/mpfi-20200401-ferret-v1-ds1. Data presented in Figure 2 and Extended Data Figure 3 are available: https://github.com/schollben/StructFuncEM2020. Additional data and published data are available from the corresponding author upon reasonable request.

Code availability

Code is available from the corresponding author upon reasonable request. NEURON modeling script is available: https://github.com/schollben/StructFuncEM2020.

Methods

All procedures were performed according to NIH guidelines and approved by the Institutional Animal Care and Use Committee at Max Planck Florida Institute for Neuroscience.

Viral Injections

Female ferrets (n = 3) aged P18–23 (Marshall Farms) were anesthetized with isoflurane (delivered in O_2). Atropine was administered and a 1:1 mixture of lidocaine and bupivacaine was administered SQ. Animals were maintained at an internal temperature of 37° Celsius.

Under sterile surgical conditions, a small craniotomy (0.8 mm diameter) was made over the visual cortex (7–8 mm lateral and 2–3 mm anterior to lambda). A mixture of diluted AAV1.hSyn.Cre (1:25000 to 1:50000) and AAV1.Syn.FLEX.GCaMP6s (UPenn) was injected (125 – 202.5 nL) through beveled glass micropipettes (10–15 μm outer diameter) at 600, 400, and 200 μm below the pia. Finally, the craniotomy was filled with sterile agarose (Type IIIa, Sigma-Aldrich) and the incision site was sutured.

Cranial Window

After 3–5 weeks of expression, ferrets were anesthetized with 50mg/kg ketamine and isoflurane. Atropine and bupivacaine were administered, animals were placed on a feedback-controlled heating pad to maintain an internal temperature of 37° Celsius, and intubated to be artificially respirated. Isoflurane was delivered throughout the surgical procedure to maintain a surgical plane of anesthesia. An intravenous cannula was placed to deliver fluids. Tidal CO_2, external temperature, and internal temperature were continuously monitored. The scalp was retracted and a custom titanium headplate adhered to the skull (Metabond, Parkell). A craniotomy was performed and the dura retracted to reveal the cortex. One piece of custom coverglass (3 mm diameter, 0.7 mm thickness, Warner Instruments) adhered to a custom insert using optical adhesive (71, Norland Products) was placed onto the brain to dampen biological motion during imaging. A 1:1 mixture of tropicamide ophthalmic solution (Akorn) and phenylephrine hydrochloride ophthalmic solution (Akorn) was applied to both eyes to dilate the pupils and retract the nictitating membranes. Contact lenses were inserted to protect the eyes. Upon completion of the surgical procedure, isoflurane was gradually reduced and pancuronium (2 mg/kg/hr) was delivered IV.

Visual Stimuli

Visual stimuli were generated using Psychopy (version 1.82)[32]. The monitor was placed 25 cm from the animal. Receptive field locations for each cell were hand mapped and the spatial frequency optimized (range: 0.04 to 0.20 cpd). For each soma and dendritic segment, square-wave or sine-wave drifting gratings were presented at 22.5 degree increments to each eye independently (2 second duration, 1 second ISI, 8–10 trials for each field of view). Drifting gratings of different directions (0 – 315°) were presented independently to both eyes.

Two-photon imaging

Two-photon imaging was performed on a Bergamo II microscope (Thorlabs) running Scanimage[33] (version 5, Vidrio Technologies) with 940 nm dispersion-compensated excitation provided by an Insight DS+ (Spectraphysics). For spine and axon imaging, power after the objective was limited to <50 mW. Cells were selected for imaging on the basis of their position relative to large blood vessels, responsiveness to visual stimulation, and lack of prolonged calcium transients resulting from over-expression of GCaMP6s. Images were collected at 30 Hz using bidirectional scanning with 512×512 pixel resolution or with custom ROIs (region of interest; framerate range: 22 – 50 Hz). Somatic imaging was performed with a resolution of 2.05 – 10.24 pixels/ μm. Dendritic spine imaging was performed with a resolution of 6.10 –15.36 pixels/μm.

Two-Photon Imaging Analysis

Imaging data were excluded from analysis if motion along the z-axis was detected. Dendrite images were corrected for in-plane motion via a 2D cross-correlation based approach in MATLAB (version 2017b) or using a piecewise non-rigid motion correction algorithm[34]. ROIs were drawn in ImageJ; dendritic ROIs spanned contiguous dendritic segments and spine ROIs were fit with custom software. Mean pixel values for ROIs were computed over the imaging time series and imported into MATLAB (version 2017b)[35]. $\Delta F/F_o$ was computed by computing F_o with time-averaged median or percentile filter (10th percentile). For spine signals, we subtracted a scaled version of the dendritic signal to remove back-propagating action potentials as performed previously[13]. A second method for isolating spine signals[36] was also employed. Briefly, dendritic signals deconvolved and an exponential filter convolved with this signal was fit to spine signals. Spine signals were then subtracted by the filtered bAP signal with the optimized parameters. $\Delta F/F_o$ traces were synchronized to stimulus triggers sent from Psychopy and collected by Spike2. Peak $\Delta F/F_o$ responses to bars and gratings were computed using the Fourier analysis to calculate mean and modulation amplitudes for each stimulus presentation, which were summed together. Spines were included for analysis if the mean peak $\Delta F/F_o$ for the preferred stimulus was >10% $\Delta F/F_o$, the SNR[9] at the preferred stimulus was > 1, and spines were weakly correlated with the dendritic signal (Spearman's correlation, r < 0.4). Some spine traces contained negative events after subtraction, so correlations were computed ignoring negative $\Delta F/F_o$ values. Preferred orientation and direction for each spine was calculated by fitting responses with a double Gaussian tuning curve[13] using lsqcurvefit (Matlab). Ocular dominance index was calculated as the normalized difference between preferred left and right eye responses[37]. Spine-soma tuning correlation was computed as the Pearson's correlation (Matlab) between mean responses a spine and mean responses of the somatic output. Orientation and direction selectivity was computed by calculating the vector strength of mean responses[38]. For local clustering analyses, trial-to-trial correlations were computed as the correlation of peak F/F responses to each stimulus on a per-trial basis. To identify spine or dendritic calcium events, F/F traces were smoothed with an exponentially weighted moving average filter (MATLAB) and locating the peaks of calcium events. Peak amplitude of calcium events were compared to the standard deviation of baseline spine fluorescence values prior to subtraction.

NEURON Modeling

For each synapse reconstructed, we simulated the change in membrane potential at the spine and soma due to a single action potential arriving at the synapse (on the spine head). Simulations of anatomical features allow generation of a single metric (voltage attenuation between spine head and soma) accounting for a variety of synapse features. This model provides an approximation, rather than taking into account the 3D geometry of synapses and diverse anatomy. The goal is to combine anatomical measurements, such as PSD area and spine neck length (Extended Data Figure 2d).

We modeled a somatic compartment (radius = 13 μm, g_{Na} = 0 S/cm^2, g_k = 0.036 S/cm^2, g_{leak} = 0.003 S/cm^2, E_{leak} = −50 mV, R_a = 105 Ωcm, C_m = 1 μF/cm^2) connected to a 400 μm long

dendrite (diameter = 1 μm, R_a = 105 Ωcm, C_m = 1 μF/cm^2). Each spine was placed on the dendrite at the distance from soma as measured with EM and connected via a 'neck' to a 'spine head' where a synapse was placed. Synapse compartments had the same basic properties (R_a = 250 Ωcm, C_m = 1 μF/cm^2) and passive conductances. Spine neck diameter was fixed to 200 nm, matching widths measured in serial EM sections (mean = 180 nm ± 75 s.d., n = 71) and the length was set to measured values. Spine neck widths were not extracted from 3D mesh volumes because, with a section thickness of 56–84 nm, thin features introduce significant errors in volume estimations, even when applying smoothing algorithms. It is important to note that given the natural variation in neck width, combined with the variation in spine anatomical and functional properties (Extended Data Figure 2), it is difficult to produce a functional synaptic weight distribution based on neck width alone (Supplementary Data 2).

Spine head length was set to 1 μm so the diameter could be determined from volume measurements (assigning spine heads to be a cylindrical compartment):

$$D = \sqrt{V/4\pi}$$

Next, we converted measured PSD area into a value describing the max synaptic conductance. Here we make several assumptions. Based on the linear correlation between the number of receptors and PSD size, we approximate ~0.87 receptors and ~2.0 receptors per 100 nm for AMPA and NMDA, respectively[39]. As a simplification, we extract PSD diameter as if our PSDs were circular (as above). Then an AMPA conductance is

$$g_{AMPA} = D_{\text{spine}} \cdot (0.87/0.100) \cdot g_R$$

where g_R is 15 pS per channel. In this way, measured PSD area is linearly related to the synaptic conductance used in each model. For each simulation, parameters were set and the maximum depolarization from V_{rest} (−67.5 mV) was measured in the somatic and spine head compartment. In this paper we only present simulations of AMPA conductance, but we also ran simulations with an additional NMDA conductance. Simulated voltage attenuation (Vm$_{\text{soma}}$/ Vm$_{\text{spine}}$) for synapses were strongly correlated (r = 0.97, p = 3.6116e-40, Spearman's correlation, one-sided test) so we expect our results to be the same for either model.

Serial Block-Face Scanning Electron Microscopy (SBF-SEM)

Five layer 2/3 pyramidal neurons from 3 animals previously imaged with *in vivo* two-photon microscopy were imaged with SBF-SEM. Following perfusion and slicing, confocal image volumes of cells imaged *in vivo* were collected on a Leica TCS SP5 II with resonant scanning running LAS AF (version 3.0, Leica). A total of 23 segments of proximal basal dendrites and 155 spines were reconstructed and analyzed. To facilitate EM reconstruction we limited imaging to proximal basal dendrites.

Fixed brain slices (2% paraformaldehyde and 2 – 2.5% glutaraldehyde in a 0.1 M sodium cacodylate buffer pH 7.4) of 80 μm thickness were trimmed to approximately 2 × 2 mm to

contain the cell of interest at the center. This was accomplished by using blood vessels and slice edges, visible in a 20x epifluorescence image of the slice, as landmarks. The tissue pieces were incubated in an aqueous solution of 2% osmium tetroxide buffered in 0.1 M sodium cacodylate for 45 minutes at room temperature (RT). Tissue was not rinsed and the osmium solution was replaced with cacodylate buffered 2.5% potassium ferrocyanide for 45 minutes at RT in the dark. Tissue was rinsed with water 2×10 minutes, which was repeated between consecutive steps. Tissue was incubated in warm (60˚C) aqueous 1% thiocarbohydrizide for 20 minutes, aqueous 1% osmium tetroxide for 45 minutes, and then 1% uranyl acetate in 25% ethanol for 20 minutes. Tissue was rinsed then left in water overnight at 4˚C. The following day, tissue was stained with Walton's lead aspartate for 30 minutes at 60˚C. Tissue was then dehydrated in a graded ethanol series (30, 50, 70, 90, 100%), 1:1 ethanol to acetone, then 100% acetone. Tissue was infiltrated using 3:1 acetone to Durcupan resin (Sigma Aldrich) for 2 hours, 1:1 acetone to resin for 2 hours, and 1:3 acetone to resin overnight, then flat embedded in 100% resin on a glass slide and covered with an Aclar sheet at 60˚C for 2 days. Since SBF-SEM requires conductive samples to minimize charging during imaging, the tissue was trimmed to less than 1×1 mm and one side was exposed using an ultramicrotome (UC7, Leica), then turned downwards to be remounted to a metal pin with conductive silver epoxy (CircuitWorks, Chemtronics).

Tissue was sectioned and imaged using a 3View2XP system (Gatan, Inc.) run by Digital Micrograph (version 3.30.1909.0, Gatan Microscopy Suite) on a Gemini SEM300 (Carl Zeiss Microscopy LLC.) equipped with an OnPoint BSE detector (Gatan, Inc.). The detector magnification was calibrated within SmartSEM imaging software (version 6.0, Carl Zeiss Microscopy LLC) and Digital Micrograph with a 500 nm cross line grating standard. A low magnification image of each block face was matched to its corresponding depth in the confocal Z-stack in Adobe Photoshop (CS6 version 13.0.1) using blood vessels and cell bodies as fiducials. These features were clear across magnification scales (from 10x to ~10,000x) and used to estimate the XY position and depth of the cell and proximal segments of basal dendrites. Final imaging was performed at 2.0–2.2 kV accelerating voltage, 20 or 30 μm aperture, working distance of ~5 mm, 0.5–1.2 μs pixel dwell time, 5.7–7 nm per pixel, knife speed of 0.1 mm/sec with oscillation, and 56 – 84 nm section thickness. Imaged volumes ranged from 125×125×36 μm to 280×170×52 μm. Pixel resolutions for each image volume (Extended Data Table 1) were calibrated following imaging with a 500 nm waffle standard using the same applied accelerating voltage and detector conditions used during imaging. Additionally, the true section thickness was measured using mitochondria diameter calibrations as previously described[40]. Calibration for each block was required, since variation in thickness can occur due to heating, charging by electron beam scanning, resin polymerization, and tissue fixation and staining quality[41,42].

Serial images were exported as TIFFs to TrakEM2 (ImageJ version 1.52p)[43] and aligned using Scale-Invariant Feature Transform image alignment with linear feature correspondences and rigid transformation[44]. Once aligned, each dendrite of interest was cropped from the full volume to reduce computational overhead in subsequent analyses. Aligned images were exported to Microscopy Image Browser (version 2.51 and 2.6)[45] for segmentation of dendrites, spines, PSDs, and boutons. Three annotators preformed segmentation on this project and the segmentations of each annotator were proof-read by an

experienced annotator (~1000 hours of segmentation experience) prior to quantification. Binary labels files were imported to Amira (versions 6.7, 2019.1) which was used to create 3D surface models of each dendrite, spine, PSD, and bouton. Each reconstructed dendrite was overlaid onto its corresponding two-photon image using Adobe Photoshop or an affine transformation was performed in Matlab for re-identification of individual spines. Amira was used to measure the volume of spine heads and boutons, surface area of PSDs, and spine neck length. Blender (versions 2.79, 2.8) was used to create 3D renderings.

Of 339 target spines preserved in EM volumes (Extended Data Table 1), 137 were not recovered (40%). Within the unrecovered group, reconstruction of 6 spines (4.4%) was abandoned due to disappearance of the spine neck or discontinuities in the neck model, 16 spines (11.7%) could not be correlated to *in vivo* targets because the targeted spine was determined to be multiple spines in the EM volume, 8 spines (5.8%) were excluded due to uncertainty in LM-EM correlation, and the remaining (78%) had no identifiable features in the EM image volume.

Human error in annotation and subsequent quantification of morphological features was estimated by independent blind reconstruction of the same dendritic segments by 3 annotators. Each annotated a total of 25 PSDs from 24 dendritic spines. From these reconstructions we quantified spine volume and PSD area. Mean standard deviation across annotators was 0.01 μm^3 and 0.05 μm^2, respectively. Examining the coefficient of variation compared to standard deviation between measurements there was no significant relationship for either spine volume (Pearson's r = 0.14, p = 0.26, one-sided test) and PSD area (Pearson's r = 0.24, p = 0.13, one-sided test).

Linear regression model

Linear regression was used to determine which factors predict trial-to-trial correlations between neighboring spines. We examined spines less than 15 μm apart and normalized dendritic distance so the range would be 0 to 1. We used $\log_{10}$ of spine volumes, as these values vary several orders of magnitude, computed a normalized size-similarity metric, and computed a functional similarity (normalized orientation preference difference between spine and soma). The predictor matrix was:

$$X = \left[\beta_1 x_d + \beta_2 \left(x_{w_1} \cdot x_{w_2} \right) + \beta_3 x_S + \beta_4 x_{\Delta\theta} + \beta_5 \left(x_{w_1} \cdot x_{w_2} \cdot x_d \cdot x_S \cdot x_{\Delta\theta} \right) \right]$$

Here x_d is normalized distances, x_w are spine sizes, x_S is the size-similarity metric, $x_{\Delta\theta}$ is the functional similarity, and β are the linear coefficients. The function fitlm (Matlab) was used to obtain coefficient weights and their significance (Extended Data Table 2).

Power Analysis

Correlations between spine-soma tuning correlation and spine volume were simulated with mvnrnd (Matlab). Spine volume data was normalized by the square root. Spine-soma tuning correlation was used because (1) these data were well approximated by a normal distribution, unlike distributions of orientation preference difference (Extended Data Figure 2), and (2) orientation preference difference and spine-soma tuning correlation are highly

related (Spearman r = −0.65, p ≈ 0, one-sided test). Simulations were run using the mean and standard deviation of each distribution, and our reported sample size (n = 155). The spearman correlation coefficient and significance (one-way test) was calculated for each simulation (10,000 iterations). Detection probability was the fraction of iterations where the correlation coefficient significance was < 0.05. Simulations were run noise-free or including measurement noise. With a 95% detection threshold, the minimum detectable correlation is 0.27 under noise-free conditions and 0.33 including measurement noise.

Statistics and reliability

Statistical analyses are described in the main text and in figure legends. We used non-parametric statistical analyses or permutation tests to avoid assumptions about the distributions of the data. All statistical analysis was performed in MATLAB. Circular-linear correlation coefficients were computed for circular variables (orientation and direction preference). For all other tests, Spearman's correlation coefficient was computed. Lilliefors test for normality was used on the data presented in Figure 3. Quantitative approaches were not used to determine if the data met the assumptions of the parametric tests.

Data presented in Figure 1 and Supplementary Data 1 is representative of all data collected from 21 dendrites from 5 cells from 3 animals. Anatomical analyses shown in Figure 1 and Supplementary Data 1 were performed independently on a total of 200 distinct synapses for this study (see Extended Data Table 1). Structure-function analyses preformed in this study were replicated independently for synaptic populations from each cell (n = 5) recovered (see Extended Data Figure 6).

Extended Data
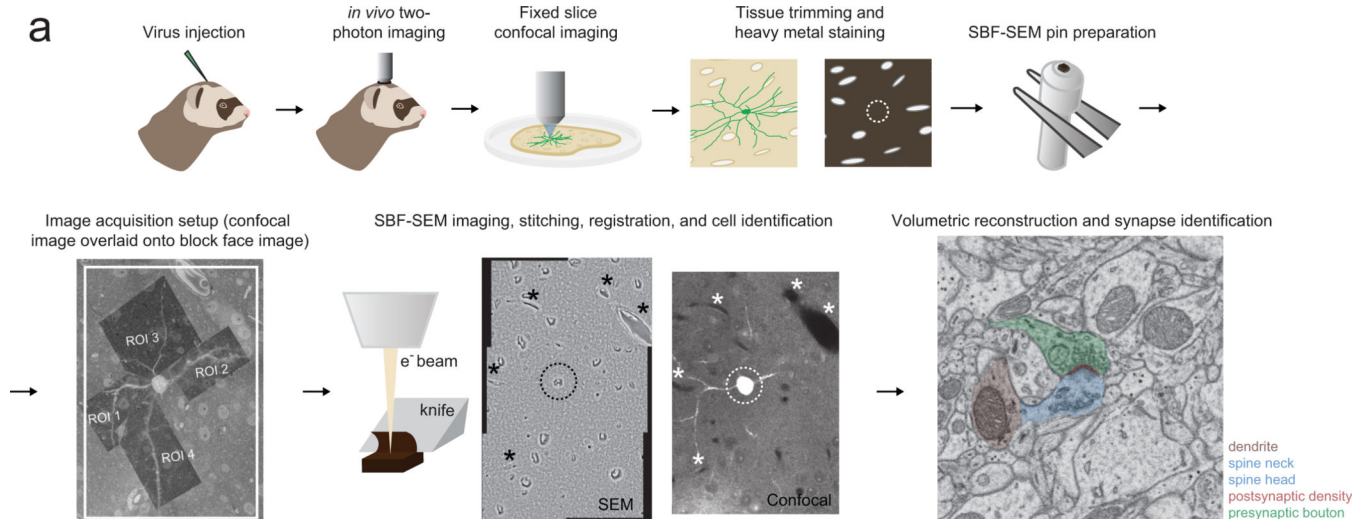
Extended Data Figure 1: Correlating *in vivo* synaptic imaging and serial block-face scanning electron microscopy.

a, Overview of correlating functional synaptic properties with ultrastructure. *In vivo* two-photon synaptic imaging of L2/3 cortical neurons in ferret visual cortex expressing GCaMP6s is performed under visual stimulation. Imaged cells are identified after perfusion

and re-imaged with a confocal microscope. Tissue is trimmed and processed for serial-block-face scanning electron microscopy (SBF-SEM). Imaged cells are identified within the block of tissue via biological fiducials and high-resolution SEM is performed. Finally, imaged cells, dendritic spines, and corresponding synaptic features are volumetrically reconstructed for quantification. Dendrite is shown in brown, spine neck and head are shown in blue, post-synaptic density is shown in red, and presynaptic bouton is shown in green.
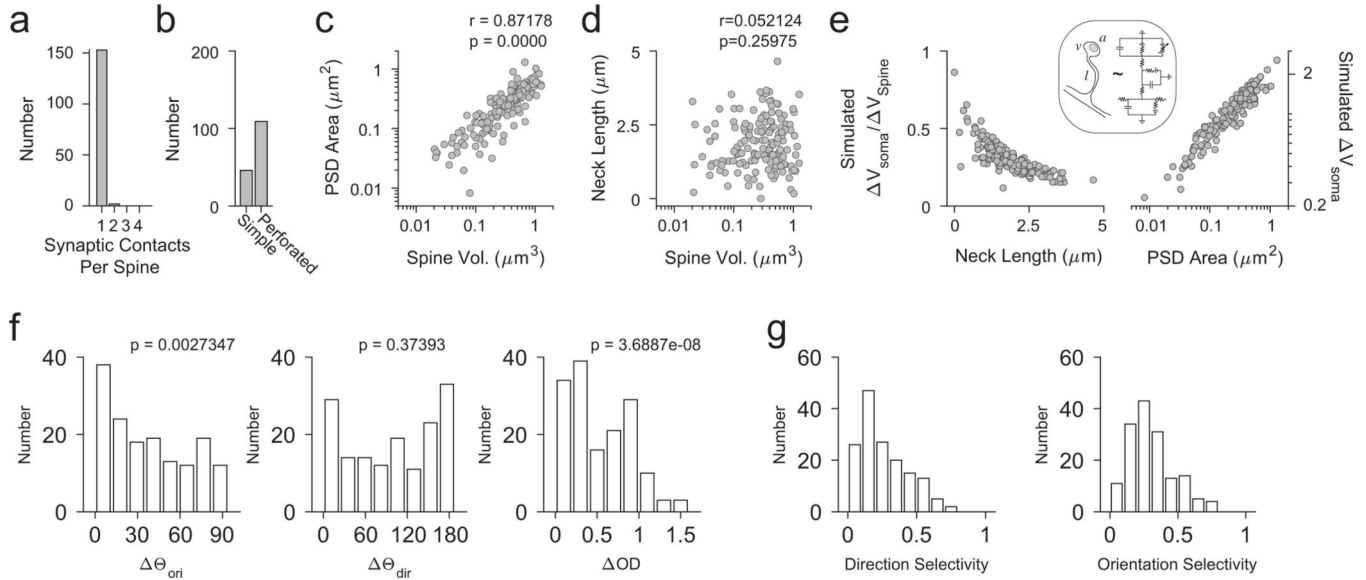
Extended Data Figure 2: Diversity of ultrastructural and functional properties for individual synapses.

a, Distribution of the number of presynaptic boutons contacting single, visually-responsive spines. **b**, Distribution of visually-responsive spines with a simple or perforated postsynaptic density (PSD). **c**, Spine head volume and PSD area are strongly correlated in individual synapses (Spearman's correlation, one-sided test, n = 155 from 5 cells). **d**, Spine head volume is not correlated with spine neck length (Spearman's correlation, two-sided test, n = 155 from 5 cells). **e**, For each synapse reconstructed, a NEURON model (Methods) was used to simulate voltage depolarization in the spine head and soma (ΔVm). A schematic of this model is shown (inset). Spines with longer necks show greater voltage attenuation (ΔVm$_{soma}$/ΔVm$_{spine}$, *left*) and spines with larger PSDs drive larger ΔVm$_{soma}$ (*right*). **f**, Distributions of spine-soma preference difference for orientation (median = 31.2, IQR = 48.4, n = 155 from 5 cells), direction (median = 106 deg, IQR = 114 deg, n = 155 from 5 cells), and ocular dominance (median = 0.43, IQR = 0.60, n = 155 from 5 cells). Except for direction preference, distributions are significantly different from a uniform distribution (Kruskal-Wallis test). **g**, Distributions of spine selectivity for direction (*left*) and orientation (*right*). Selectivity computed as vector strength (Methods) of peak responses elicited by stimulation of the preferred eye.
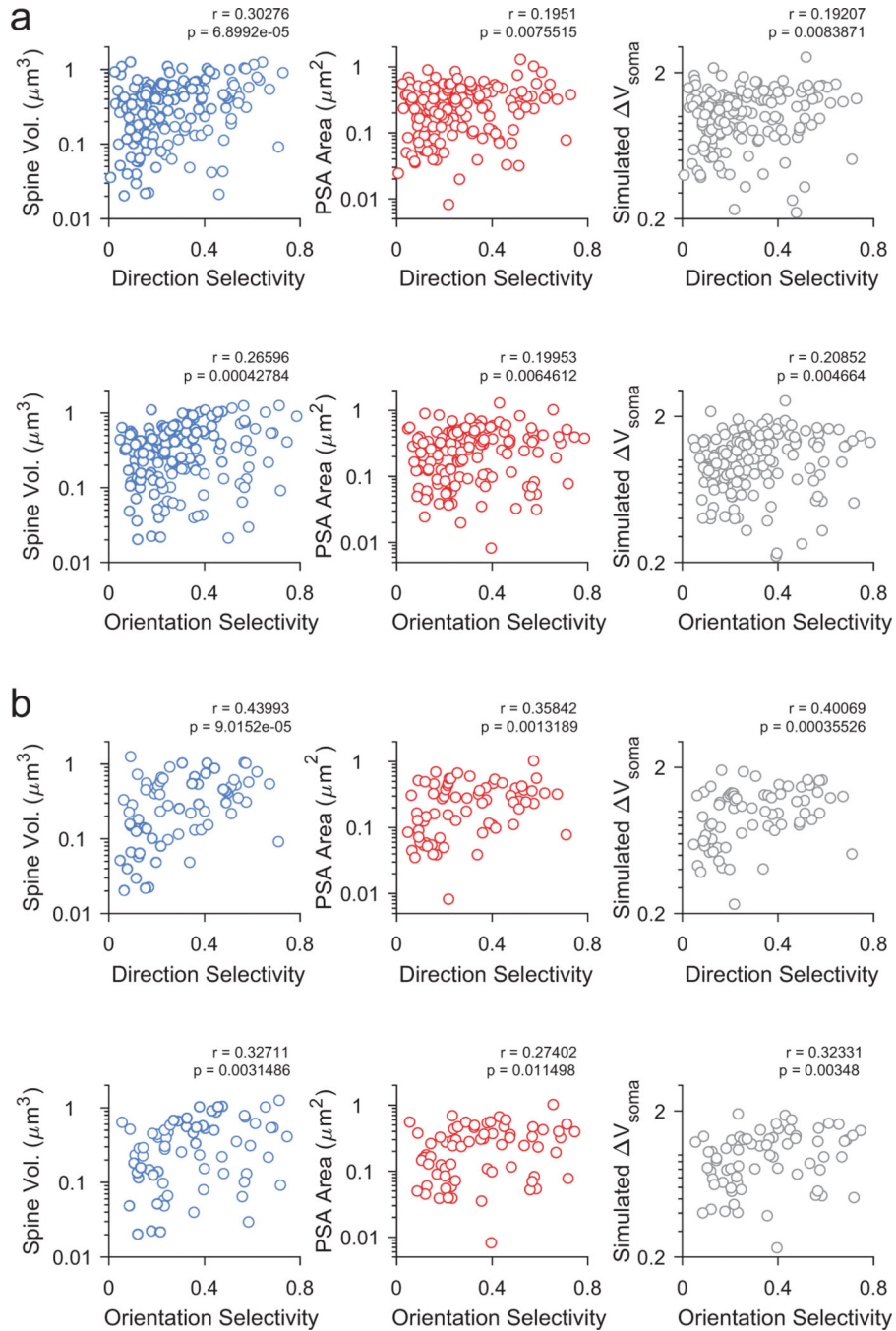
Extended Data Figure 3: Spine-soma functional similarity is uncorrelated with synaptic strength.
Relationships between the difference in direction preference (*top*), ocular dominance (*middle*), and tuning correlation (*bottom*) with synapse spine head volume (*blue*), PSD area (*red*), and simulated spine-some voltage attenuation (*gray*). Above each plot, correlation magnitude and p-value is shown. For direction preference difference, Circular-Linear correlation coefficient was calculated. For ocular dominance and tuning correlation, Spearman's correlation coefficient was calculated. All significance tests are one-sided.
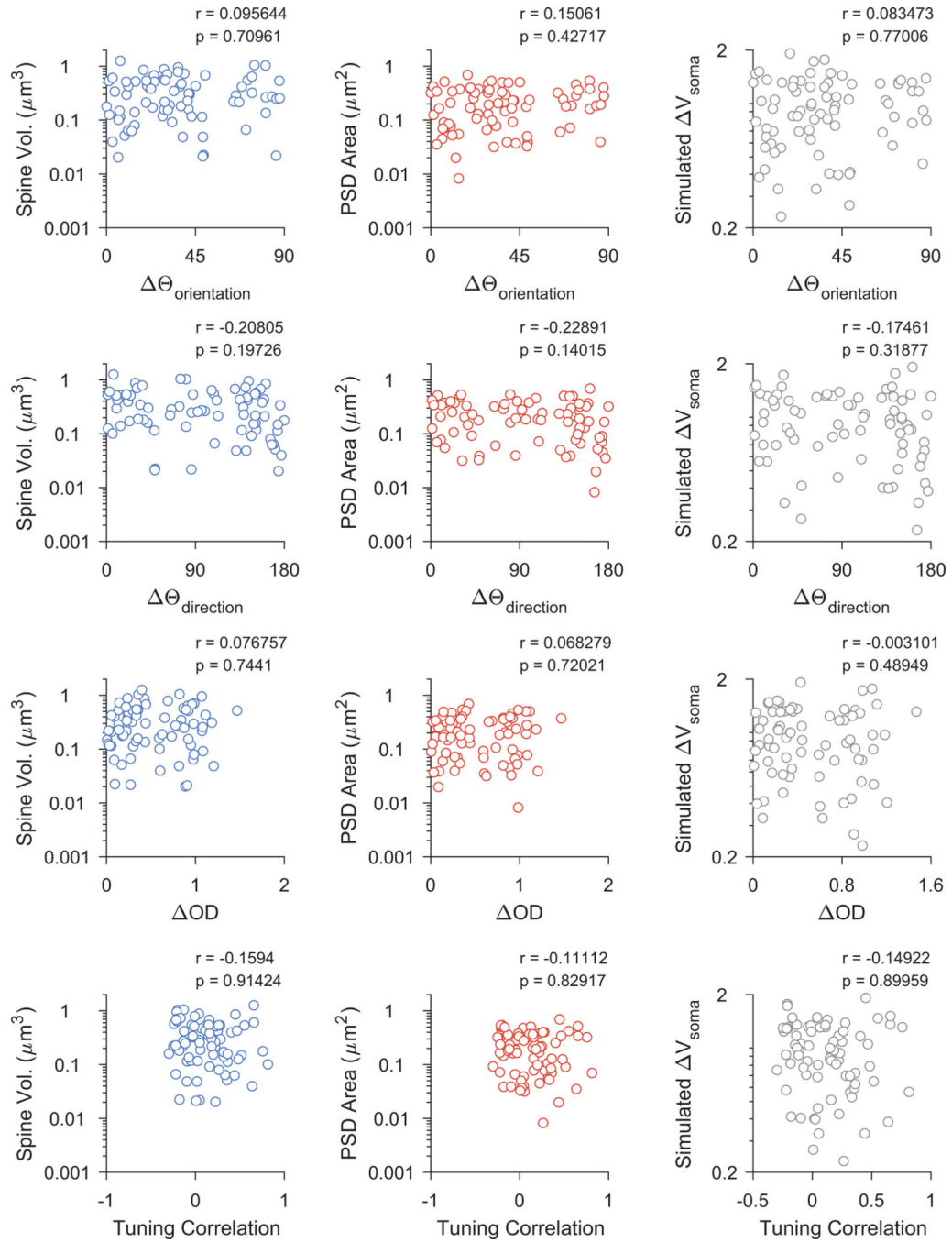
Extended Data Figure 4: Spine-soma functional similarity is uncorrelated with synaptic strength for spines with low residual correlation with dendritic signals.

Relationships between the difference in orientation preference, direction preference, ocular dominance, and tuning correlation with spine head volume (*blue*), PSD area (*red*), and simulated spine-some voltage attenuation (*gray*). Spines included were required to have $r_{residual} < 0.2$. Above each plot, correlation magnitude and p-value is shown. For orientation and direction preference differences, Circular-Linear correlation coefficient was calculated. For ocular dominance and tuning correlation, Spearman's correlation coefficient was calculated. All significance tests are one-sided.
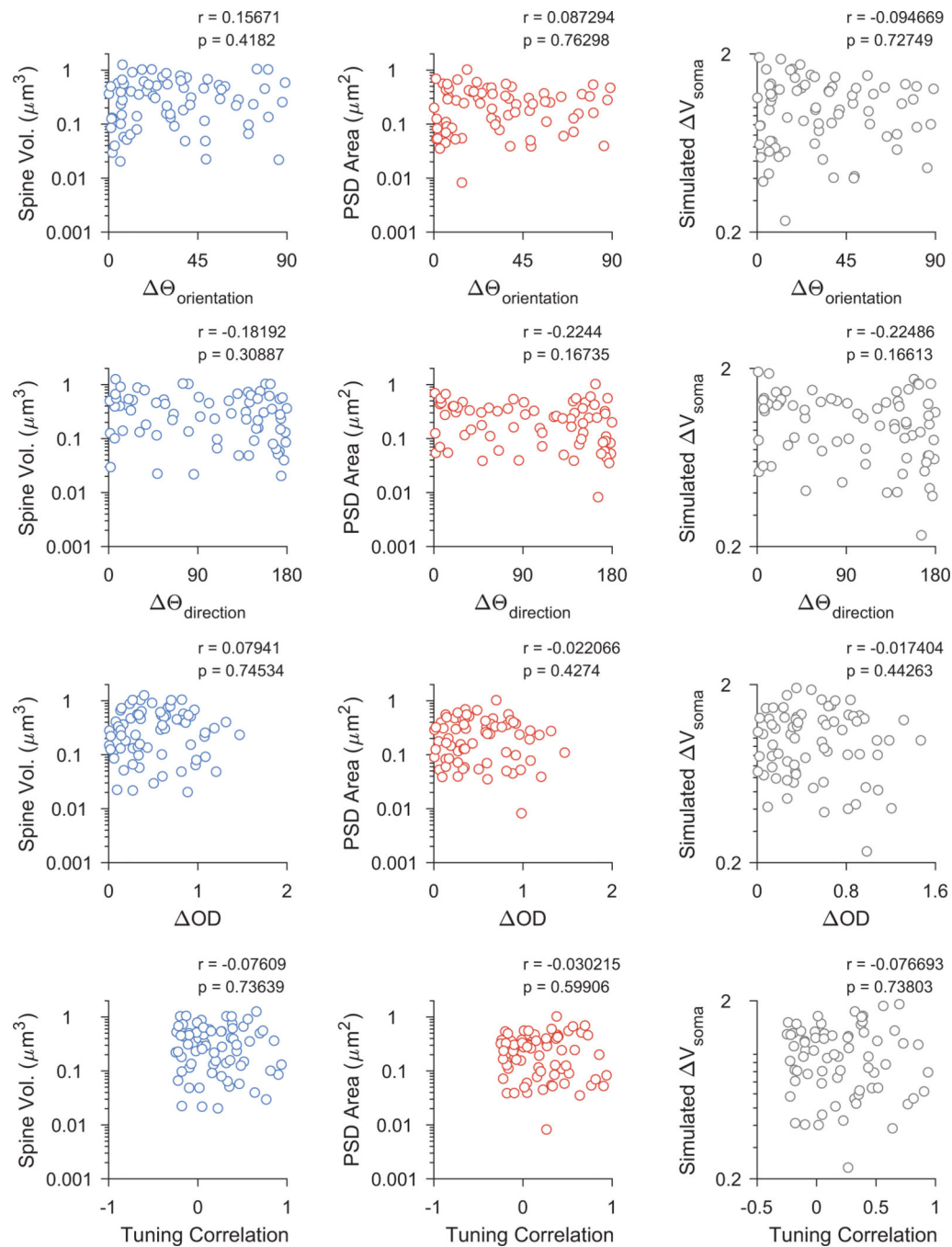
Extended Data Figure 5: Spine-soma functional similarity is uncorrelated with synaptic strength for spines with high SNR.
Relationships between the difference in orientation preference, direction preference, ocular dominance, and tuning correlation with spine head volume (*blue*), PSD area (*red*), and simulated spine-some voltage attenuation (*gray*). Spines included were required to have an SNR > 3. Above each plot, correlation magnitude and p-value is shown. For orientation and direction preference differences, Circular-Linear correlation coefficient was calculated. For ocular dominance and tuning correlation, Spearman's correlation coefficient was calculated. All significance tests are one-sided.
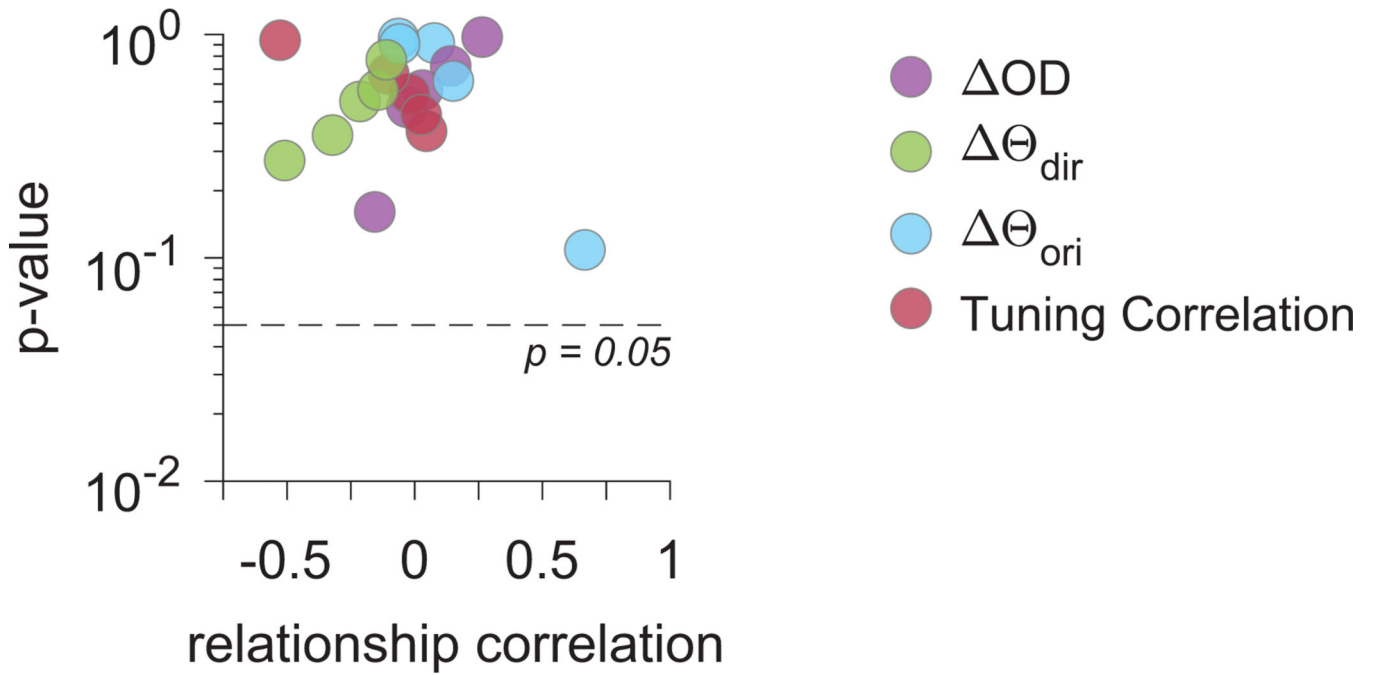
Extended Data Figure 6: Relationship between spine-soma orientation preference and synaptic strength across cell populations.

Shown are the correlation coefficient (abscissa) and associated p-value (ordinate) for spine population on each cell imaged and reconstructed. The color of each data point represents the functional property examined. For orientation and direction preference differences, Circular-Linear correlation coefficient was calculated. For ocular dominance and tuning correlation, Spearman's correlation coefficient was calculated. Dashed line is p = 0.05 cutoff. All significance tests are one-sided.
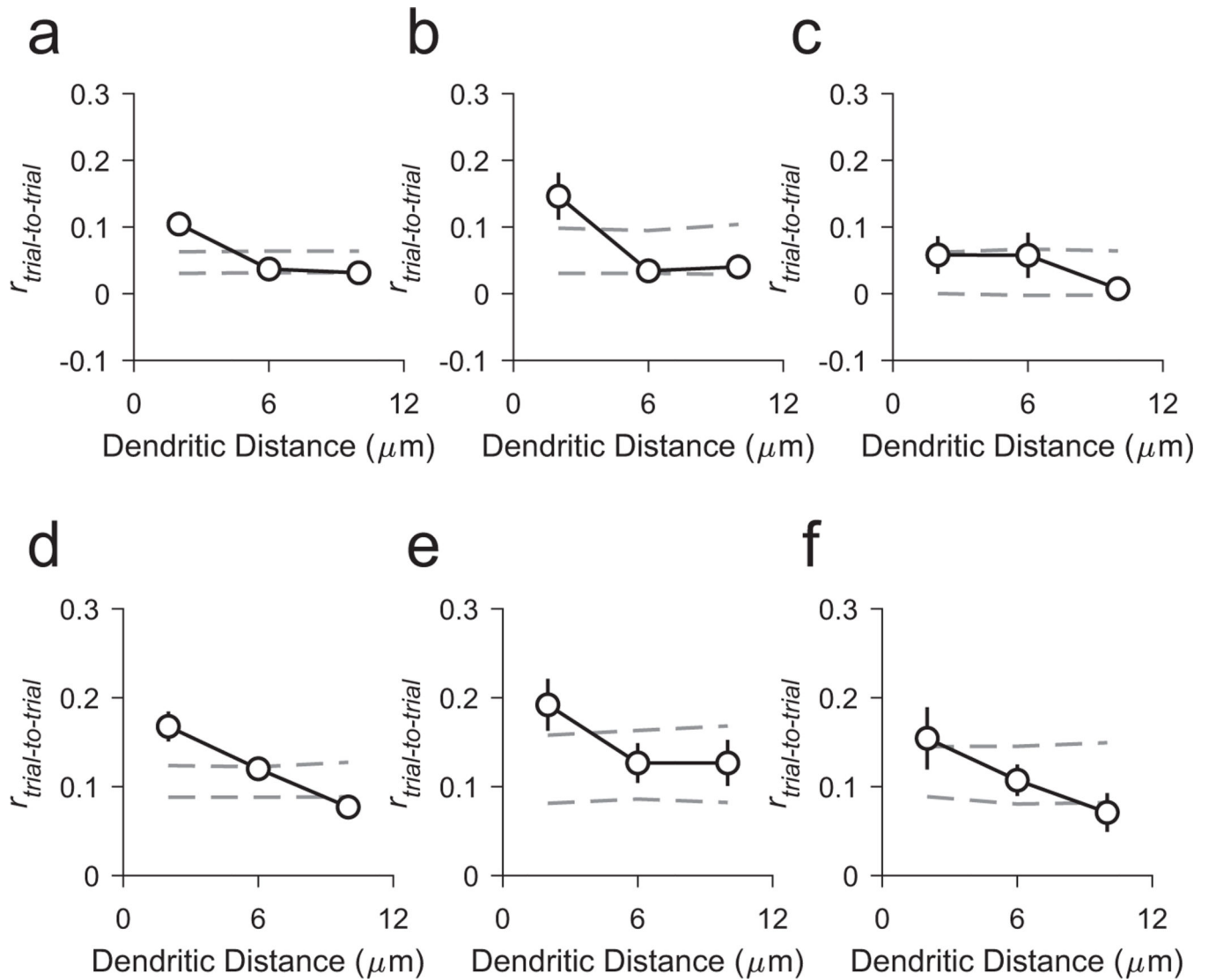
Extended Data Figure 7: Spatiotemporal clustering of synaptic events excluding bAPs and comparing spine neck length.

a, Relationship between spine pair distance and trial-to-trial correlation during visual stimulation, excluding stimulus trials with dendritic calcium events (Methods). Data are mean and standard error (*black*). Also shown are shuffled correlations (*gray dashed lines*), data are SEM (n = 396 pairs from 5 cells). **b**, Same as in (a) for synapse pairs with smaller spine head volume (< 0.35 μm^3; n = 132 pairs from 5 cells). **c**, Same as in (a) for synapse pairs with larger spine head volumes (> 0.35 μm^3; n = 86 pairs from 5 cells). **d**, Relationship between spine pair distance and trial-to-trial correlation during visual stimulation. Note, these data are the same as shown in Figure 4a. **e**, Same as in (**d**) for synapse pairs with smaller neck lengths (< 1.75 μm; n = 112 pairs from 5 cells). **f**, Same as in (**d**) for synapse pairs with longer neck lengths (< 1.75 μm; n = 106 pairs from 5 cells).
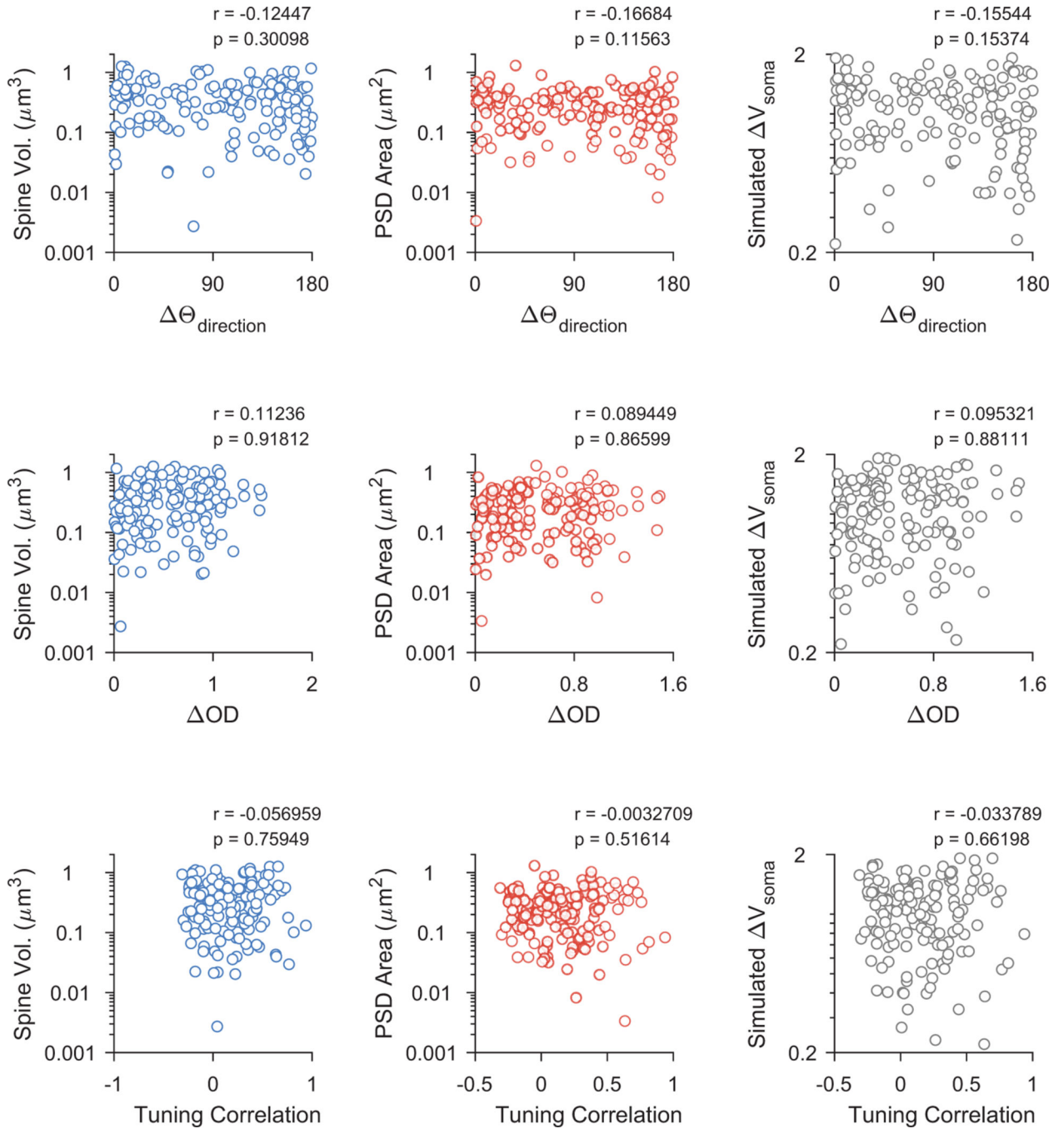
Extended Data Figure 8: Visual selectivity is correlated with synaptic strength.
a, Relationship between spine selectivity (vector strength) for direction (*top*) and orientation (*bottom*) and spine head volume (*blue*), PSD area (*red*), and simulated spine-some voltage attenuation (*gray*). Above each plot, Spearman's correlation coefficient and significance (one-sided test) is shown. **b**, Same as in (a), but for spines with SNR > 3. Note that correlation significance persists and for some comparisons, the correlation magnitude is larger.

Extended Data Table 1:
Anatomical statistics.

Description of EM imaging parameters, volumes, and synaptic reconstructions.

Cells Reconstructed	**5**
Imaging voxel size and accelerating voltage	
Cell 1	7.0×7.0×67 nm, 2.2kV
Cell 2	6.0×6.0×68 nm, 2.0kV
Cell 3	5.7×5.7×56 nm, 2.2kV
Cell 4	5.7×5.7×62 nm, 2.0kV
Cell 5	5.7×5.7×84 nm, 2.2kV
Dendrites reconstructed	**23**
Total length	1,688 μm
Segment length (mean ± s.d.)	76.71 ± 40.90 μm
Target synapses	**372**
Preserved in EM volume	339
Unrecovered target spines	137
Abandoned reconstruction	6
Abandoned Correlation	8
Target was multiple spines	16
No features in EM volume	78
Target synapses reconstructed	**200**
Spines with PSDs	200
Spines with >1 presynaptic input	8
Functionally characterized reconstructions	**155**
Spines with PSDs	155
Spines with >1 presynaptic input	2
Spine volume range	$0.0027 - 1.26\ \mu m^3$
PSD area range	$0.0034 - 1.30\ \mu m^2$
Bouton volume range	$0.0116 - 1.59\ \mu m^3$
Spine neck length range	$0 - 4.65\ \mu m$

Extended Data Table 2:
Linear regression model predicting pairwise
spatiotemporal correlations between nearby spines.

Shown (from left to right) are regression coefficients, coefficient descriptions, coefficient magnitude, and coefficient significance (p-value). Significance reported is a two-sided t-statistic testing whether coefficient magnitude is different from zero.

Coefficient	Description	Estimate	p-value
β_1	Dendritic distance	−0.07	1.6e-2
β_2	Volume	0.08	2.8e-4
β_3	Volume similarity	0.03	0.34

Coefficient	Description	Estimate	p-value
β_4	Spine-soma orientation preference difference	−0.01	0.86
β_5	Full-interaction	−0.42	5.5e-3

Supplementary Material

Refer to Web version on PubMed Central for supplementary material.

Acknowledgements:

References

1. Miller KD in Models of neural networks III (eds. Domany E, Hemmen JL & Schulten K.) 55–78 (Springer New York, 1996). doi:10.1007/978-1-4612-0723-8_2

2. Abbott LF & Nelson SB Synaptic plasticity: taming the beast. Nat. Neurosci 3 Suppl, 1178–1183 (2000). [PubMed: 11127835]

3. Bartol TM et al. Nanoconnectomic upper bound on the variability of synaptic plasticity. Elife 4, e10778 (2015).

4. Harris KM Structure, development, and plasticity of dendritic spines. Curr. Opin. Neurobiol 9, 343–348 (1999). [PubMed: 10395574]

5. Tanaka J-I et al. Protein synthesis and neurotrophin-dependent structural plasticity of single dendritic spines. Science 319, 1683–1687 (2008). [PubMed: 18309046]

6. Cossell L. et al. Functional organization of excitatory synaptic strength in primary visual cortex. Nature 518, 399–403 (2015). [PubMed: 25652823]

7. Lee W-CA et al. Anatomy and function of an excitatory network in the visual cortex. Nature 532, 370–374 (2016). [PubMed: 27018655]

8. El-Boustani S. et al. Locally coordinated synaptic plasticity of visual cortex neurons in vivo. Science 360, 1349–1354 (2018). [PubMed: 29930137]

9. Scholl B, Wilson DE & Fitzpatrick D. Local Order within Global Disorder: Synaptic Architecture of Visual Space. Neuron 96, 1127–1138.e4 (2017).

10. Denk W. & Horstmann H. Serial block-face scanning electron microscopy to reconstruct three-dimensional tissue nanostructure. PLoS Biol. 2, e329 (2004).

11. Arellano JI, Benavides-Piccione R, Defelipe J. & Yuste R. Ultrastructure of dendritic spines: correlation between synaptic and spine morphologies. Front. Neurosci 1, 131–143 (2007). [PubMed: 18982124]

12. Kasthuri N. et al. Saturated reconstruction of a volume of neocortex. Cell 162, 648–661 (2015). [PubMed: 26232230]

13. Wilson DE, Whitney DE, Scholl B. & Fitzpatrick D. Orientation selectivity and the functional clustering of synaptic inputs in primary visual cortex. Nat. Neurosci 19, 1003–1009 (2016). [PubMed: 27294510]

14. Hering H. & Sheng M. Dendritic spines: structure, dynamics and regulation. Nat. Rev. Neurosci 2, 880–888 (2001). [PubMed: 11733795]

15. Bourne JN & Harris KM Coordination of size and number of excitatory and inhibitory synapses results in a balanced structural plasticity along mature hippocampal CA1 dendrites during LTP. Hippocampus 21, 354–373 (2011). [PubMed: 20101601]

16. Toni N, Buchs PA, Nikonenko I, Bron CR & Muller D. LTP promotes formation of multiple spine synapses between a single axon terminal and a dendrite. Nature 402, 421–425 (1999). [PubMed: 10586883]

17. Araya R, Jiang J, Eisenthal KB & Yuste R. The spine neck filters membrane potentials. Proc. Natl. Acad. Sci. USA 103, 17961–17966 (2006). [PubMed: 17093040]

18. Hines ML, Davison AP & Muller E. NEURON and Python. Front Neuroinformatics 3, 1 (2009).

19. Sobczyk A, Scheuss V. & Svoboda K. NMDA receptor subunit-dependent [Ca2+] signaling in individual hippocampal dendritic spines. J. Neurosci 25, 6037–6046 (2005). [PubMed: 15987933]

20. Losonczy A. & Magee JC Integrative properties of radial oblique dendrites in hippocampal CA1 pyramidal neurons. Neuron 50, 291–307 (2006). [PubMed: 16630839]

21. Harvey CD & Svoboda K. Locally dynamic synaptic learning rules in pyramidal neuron dendrites. Nature 450, 1195–1200 (2007). [PubMed: 18097401]

22. Buzsáki G. & Mizuseki K. The log-dynamic brain: how skewed distributions affect network operations. Nat. Rev. Neurosci 15, 264–278 (2014). [PubMed: 24569488]

23. Hofer SB, Mrsic-Flogel TD, Bonhoeffer T. & Hübener M. Experience leaves a lasting structural trace in cortical circuits. Nature 457, 313–317 (2009). [PubMed: 19005470]

24. Kirchner JH & Gjorgjieva J. A unifying framework for synaptic organization on cortical dendrites. BioRxiv (2019). doi:10.1101/771907

25. Alonso A, de Curtis M. & Llinás R. Postsynaptic Hebbian and non-Hebbian long-term potentiation of synaptic efficacy in the entorhinal cortex in slices and in the isolated adult guinea pig brain. Proc. Natl. Acad. Sci. USA 87, 9280–9284 (1990). [PubMed: 1979169]

26. Nishiyama J. & Yasuda R. Biochemical computation for spine structural plasticity. Neuron 87, 63–75 (2015). [PubMed: 26139370]

27. Feldmeyer D, Egger V. & Joachim. Reliable synaptic connections between pairs of excitatory. J. Physiol. (Lond.) 521(1), 169–190. [PubMed: 10562343]

28. Feldmeyer D, Lübke J, Silver RA & Sakmann B. Synaptic connections between layer 4 spiny neurone-layer 2/3 pyramidal cell pairs in juvenile rat barrel cortex: physiology and anatomy of interlaminar signalling within a cortical column. J. Physiol. (Lond.) 538, 803–822 (2002). [PubMed: 11826166]

29. Markram H, Lübke J, Frotscher M, Roth A. & Sakmann B. Physiology and anatomy of synaptic connections between thick tufted pyramidal neurones in the developing rat neocortex. J. Physiol. (Lond.) 500(Pt 2), 409–440 (1997). [PubMed: 9147328]

30. Holler-Rickauer S, Koestinger G, Martin KAC, Schuhknecht GFP & Stratford KJ Structure and function of a neocortical synapse. BioRxiv (2019). doi:10.1101/2019.12.13.875971

31. Nicholson DA et al. Distance-dependent differences in synapse number and AMPA receptor expression in hippocampal CA1 pyramidal neurons. Neuron 50, 431–442 (2006). [PubMed: 16675397]

Methods References

32. Peirce JW PsychoPy--Psychophysics software in Python. J. Neurosci. Methods 162, 8–13 (2007). [PubMed: 17254636]

33. Pologruto TA, Sabatini BL & Svoboda K. ScanImage: flexible software for operating laser scanning microscopes. Biomed Eng Online 2, 13 (2003). [PubMed: 12801419]

34. Pnevmatikakis EA & Giovannucci A. NoRMCorre: An online algorithm for piecewise rigid motion correction of calcium imaging data. J. Neurosci. Methods 291, 83–94 (2017). [PubMed: 28782629]

35. Sage D, Prodanov D. & Tinevez JY MIJ: making interoperability between ImageJ and Matlab possible. bigwww.epfl.ch (2012).

36. Kerlin A. et al. Functional clustering of dendritic activity during decision-making. Elife 8, (2019).

37. Scholl B, Pattadkal JJ, Dilly GA, Priebe NJ & Zemelman BV Local integration accounts for weak selectivity of mouse neocortical parvalbumin interneurons. Neuron 87, 424–436 (2015). [PubMed: 26182423]

38. Scholl B, Tan AYY, Corey J. & Priebe NJ Emergence of orientation selectivity in the Mammalian visual pathway. J. Neurosci 33, 10616–10624 (2013). [PubMed: 23804085]

39. Takumi Y, Ramírez-León V, Laake P, Rinvik E. & Ottersen OP Different modes of expression of AMPA and NMDA receptors in hippocampal synapses. Nat. Neurosci 2, 618–624 (1999). [PubMed: 10409387]

40. Fiala JC & Harris KM Cylindrical diameters method for calibrating section thickness in serial electron microscopy. J. Microsc 202, 468–472 (2001). [PubMed: 11422668]

41. Starborg T. et al. Using transmission electron microscopy and 3View to determine collagen fibril size and three-dimensional organization. Nat. Protoc 8, 1433–1448 (2013). [PubMed: 23807286]

42. Hughes L, Hawes C, Monteith S. & Vaughan S. Serial block face scanning electron microscopy--the future of cell ultrastructure imaging. Protoplasma 251, 395–401 (2014). [PubMed: 24240569]

43. Cardona A. et al. TrakEM2 software for neural circuit reconstruction. PLoS One 7, e38011 (2012).

44. Lowe G. SIFT-the scale invariant feature transform. Int. J (2004).

45. Belevich I, Joensuu M, Kumar D, Vihinen H. & Jokitalo E. Microscopy image browser: A platform for segmentation and analysis of multidimensional datasets. PLoS Biol. 14, e1002340 (2016).
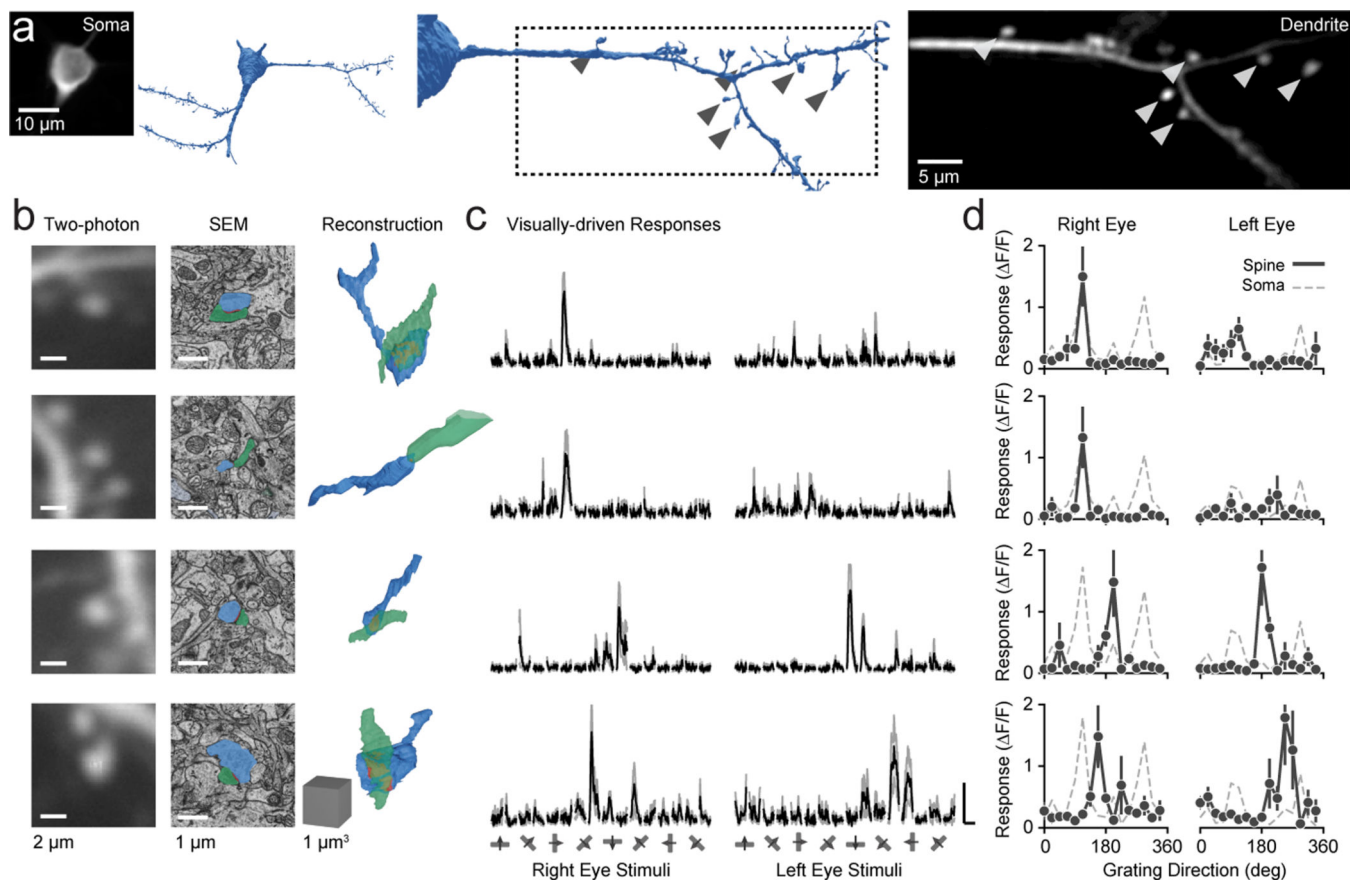
Figure 1: Correlating *in vivo* synaptic imaging and serial block-face scanning electron microscopy.

a, Example neuron imaged and reconstructed. Shown is a two-photon average-projection of the soma (*left*) and dendrite (*right*). Reconstructions of this cell shown in blue. Reconstructed PSDs and presynaptic boutons not shown. Arrows denote visually-responsive spines identified in the EM reconstruction. **b**, Example representative spines imaged and corresponding EM reconstructions. Shown are a two-photon average-projection (*left column*), single electron micrograph with annotations (*middle column*), and the full EM model *(right column)*. Colors indicate spine head and neck (*blue*), PSD (*red*), and presynaptic bouton (*green*). **c**, Calcium responses driven by visual stimuli for each spine in (b). Data are mean (black) and standard error (gray) (n = 8 stimulus trials). Scale is 100% F/F and 3 sec. **d**, Peak F/F responses across visual stimuli for each spine in (b). Spine data are mean and standard error (n = 8 stimulus trials). Shown also are mean responses of the soma of this cell (gray, dashed line).
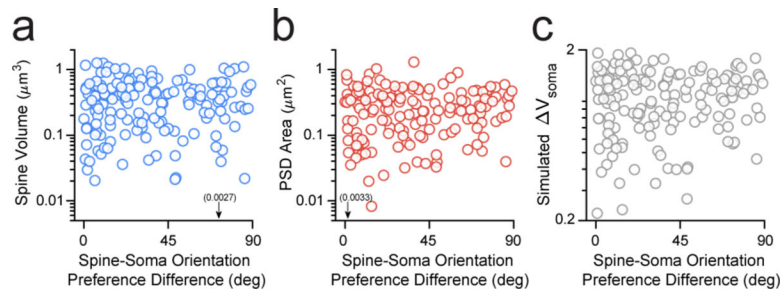
Figure 2: Similarity in spine-soma orientation preference is uncorrelated with synaptic strength.
a, Spine head volume is uncorrelated with difference in orientation preference between each spine and corresponding soma (Circular-linear r = 0.03, p = 0.91, one-sided test). Each data point (*blue*) represents an individual visually-responsive synapse reconstructed (n = 155 from 5 cells). Arrow denotes a data point outside ordinate limits. **b**, Same as in (a) for PSD area (*red*; Circular-linear r = 0.12, p = 0.34, one-sided test). **c**, Same as in (a) for NEURON simulation of somatic depolarization for each spine reconstructed (*gray*; Circular-linear r = 0.08, p = 0.60, one-sided test). Note ordinate scale is linear.
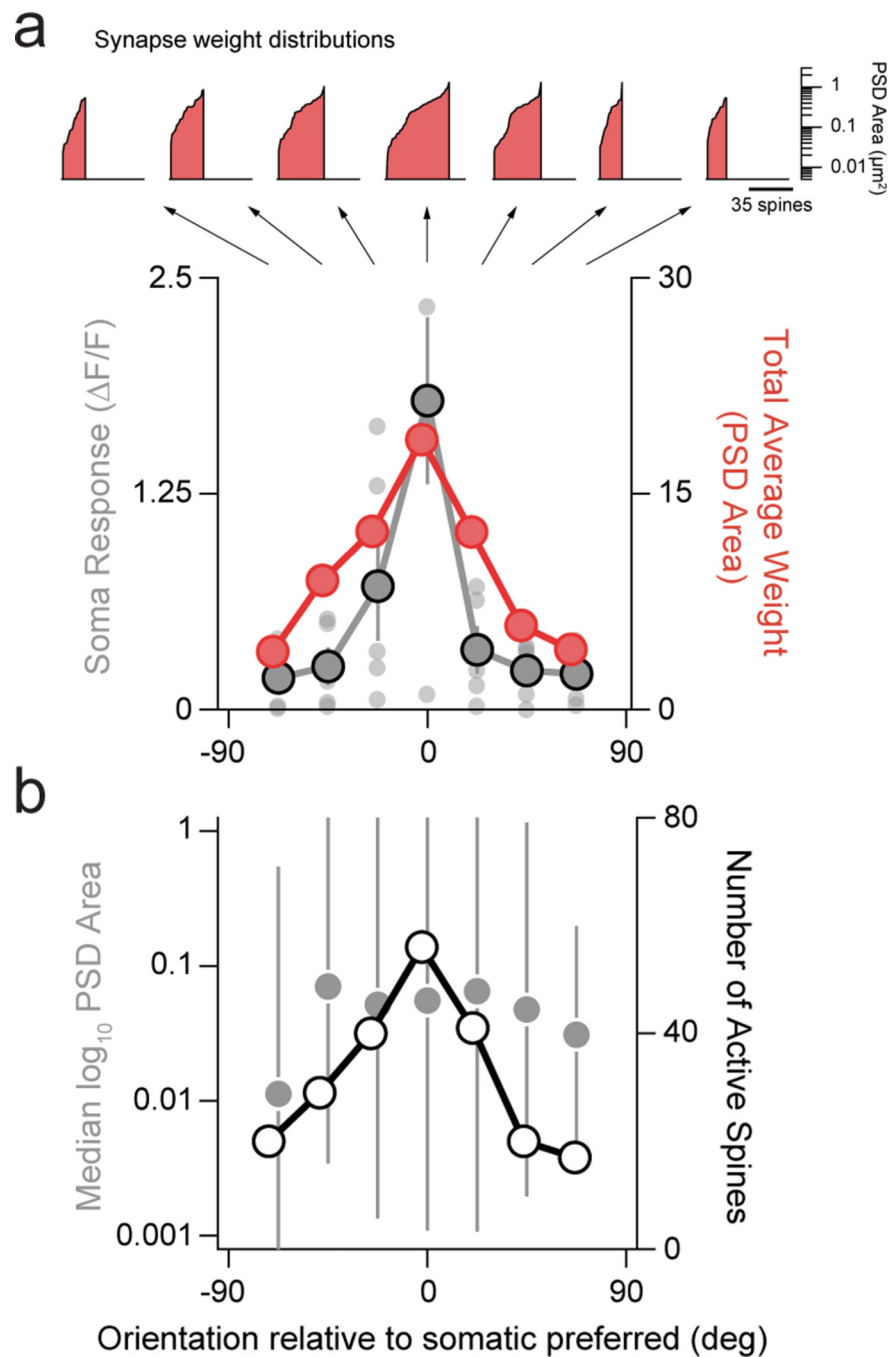
Figure 3: Somatic selectivity predicted by total weight derived from total number of active synapses.

a, Average somatic orientation tuning (n = 5 cells, *gray*) compared to the total average weight (summed PSD area, *red*) from active synapses for each stimulus condition ($\theta_{soma\ pref}$ ± 67.5°). Active synapses defined as those exhibiting calcium events on at least 50% of stimulus presentation trials. Soma data are individual data points, mean, and standard error. Total weight is summed PSD area across active spines. Shown at top are cumulative distributions of PSD area for active synapses for each stimulus condition. Note, ordinate is

PSD area (μm^2) and abscissa is total number of active spines. **b**, Plots of median $\log_{10}$ PSD area and interquartile range across active spines (gray circles) and total number of active spines (white circles) for each orientation. Data derive from distributions shown in **a**.
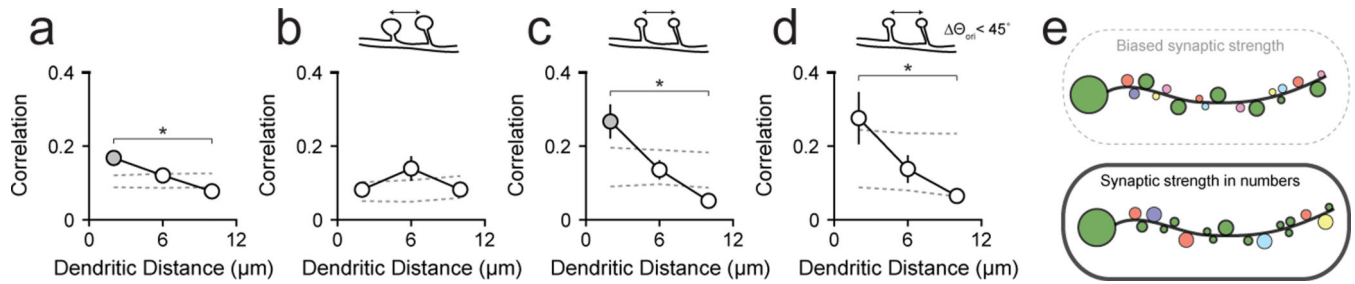
Figure 4: Smaller, but not larger, synapses exhibit local spatiotemporal clustering.
a, Relationship between spine pair distance and trial-to-trial correlation during visual stimulation. Data are mean and SEM (*black*; n = 396 pairs from 5 cells). Also shown is shuffle correlation SEM (*gray dashed lines*). Gray data point denotes significant difference from shuffled correlations (p = 0.002, bootstrapped confidence interval, one-sided test). Asterisk denotes significantly different correlation distributions (p = 0.000048, Wilcoxon rank-sum two-sided test). **b**, Same as in (a) for large synapse pairs (volume > 0.35 μm^3; n = 102 pairs from 5 cells). **c**, Same as in (a) for small synapse pairs (volume < 0.35 μm^3; n = 104 pairs from 5 cells). Gray data point denotes significant difference from shuffle (p = 0.012, bootstrapped confidence interval, one-sided test). Asterisk denotes significantly different correlation distributions (p = 0.000052, Wilcoxon rank-sum two-sided test). **d**, Same as in (a) for small synapse pairs co-tuned with the somatic output ($\theta_{pref} < 45°$; n = 46 pairs from 5 cells). Asterisk denotes significantly different correlation distributions (p = 0.025, Wilcoxon rank-sum two-sided test). Nearest pairs trended towards greater correlation than shuffle (p = 0.051, bootstrapped confidence interval, one-sided test). **e**, Illustration of two competing models of the synaptic basis for response selectivity. Our data do not support functionally-biased synaptic strength (*top*). Instead, our data suggest strength in numbers (*bottom*) whereby inputs co-tuned with the soma are more numerous but exhibit a wide range of strengths.